Effects of gas phase ion irradiation and vacuum annealing on the visible light photocatalytic properties of WO_3

Yuki Nakagawa,[a*] Yuya Hayashi,[b] Subing Yang,[a] Tamaki Shibayama[a]

[a] Faculty of Engineering, Hokkaido University, N-13, W-8, Sapporo, 060-8628, Japan

[b] Graduate School of Engineering, Hokkaido University, N-13, W-8, Sapporo, 060-8628, Japan

ABSTRACT

Oxygen vacancies were introduced into tungsten oxide (WO_3) rods by irradiation with H_2^+, He^+ or Ar^+ ions and/or vacuum annealing. The surface chemical bonding states and visible light photocatalytic properties of these materials were subsequently assessed. Although the irradiated surfaces were contaminated with carbon and silicon species during ion irradiation, vacuum annealing at 500 °C decreased the extent of carbon contamination and increased the concentration of lattice oxygen species related to a surface WO_{3-x} phase. The irradiated WO_{3-x} rods exhibited low photocatalytic efficiencies during the degradation of rhodamine 6G compared with pristine WO_3 rods, possibly due to the existence of contamination and oxygen vacancies. Vacuum-annealed WO_{3-x} rods having a green coloration exhibited high photocatalytic efficiency as a result of enhanced visible light absorption and the low concentration of both surface contamination and vacancies.

Keywords: tungsten oxide, ion irradiation, vacuum annealing, carbon contamination, oxygen vacancy, photocatalysis

1. Introduction

Tungsten oxide (WO_3) has attracted much attention as a photocatalyst [1,2] and as a component of gas sensors [3], surface-enhanced Raman scattering (SERS) sensors [4,5] and photochromic devices [6,7]. This oxide has a narrow band gap of 2.5 eV and is known to function as an efficient visible-light-active photocatalyst. A nonstoichiometric tungsten oxide phase (WO_{3-x}) can also be synthesized by annealing [8,9], chemical vapor deposition [10] or ion irradiation [11-14]. In addition, the nuclear collisions occurring during ion irradiation of the oxide can generate oxygen vacancies that act as donor defects. The introduction of oxygen vacancies into WO_3 can change its coloration from yellow to blue [14], suggesting applications as a chromic material. Like WO_{3-x}, tungsten bronze (H_xWO_3) displays a blue color and thus has various electrochromic uses [15,16]. In fact, WO_{3-x} thin films fabricated by ion irradiation have a number of unique properties that may allow for various applications. As an example, WO_{3-x} thin films synthesized by Ar^+ irradiation followed by vacuum annealing exhibit excellent SERS sensitivity [17]. In addition, the room temperature ferromagnetism of tungsten oxide films is enhanced by Ar^+ irradiation [18]. It has also been reported that the methane gas-sensing properties of these materials are improved by Ar^+ irradiation [19]. Surface reduction of tungsten oxide nanowire film was also performed by Ar^+ bombardment with low ion beam voltage to produce uniform tungsten corn arrays [20].

The effects of ion irradiation on photocatalytic properties of WO_3 has not been clarified yet. In the case of photocatalysis, oxygen vacancies have been shown to have both positive and negative effects. WO_{3-x} nanoparticles synthesized via a plasma incident on a liquid [21], thermal reduction by H_2 gas [22] and low temperature annealing in an alcohol [23] have exhibited enhanced organic dye photodegradation properties. In addition, WO_{3-x} nanoparticles synthesized via hydrogen plasma treatment showed enhanced photocatalytic O_2 evolution properties from water oxidation [24]. Conversely, WO_{3-x} nanoparticles produced under a mixture of gaseous H_2 and N_2 did not decompose acetaldehyde [25]. Vacuum-annealed WO_{3-x} particles have also shown different photocatalytic properties depending on the annealing temperature. Specifically, samples treated at low and high temperatures have demonstrated excellent and poor promotion of the water oxidation reaction, respectively [26]. For considering the effects of ion irradiation on photocatalytic properties, carbon contamination on the surface of the catalysts also should be examined. It has been known that carbon incorporation often occurs during ion irradiation [27,28]. In our previous study, carbon contamination was also introduced by He^+ irradiation and subsequent effects of

thermal oxidation of Cu was verified [29]. Also, He^+ irradiation and the carbon contamination introduction into Cu showed the rapid growth of CuO during the subsequent oxidation in alkaline solution conditions [30].

In the present study, WO_3 rods were synthesized and then irradiated with either H_2^+, He^+ or Ar^+ ions at room temperature. We selected different kinds of gas phase ions and compared their effects on defects amounts and microstructure evolutions. In applications involving photocatalysis or SERS, it is important to control surface defects and contaminations. Thus, both pristine and irradiated rods were subjected to vacuum annealing. The surface structures, bonding states and visible light photocatalytic properties of the resulting materials were investigated. The relationships between the defect introduction process and visible light photocatalytic properties are discussed herein based on the results observed.

2. Material and methods

2.1. Sample Synthesis

Tungsten rods (φ 2 mm, purity 99.95%) were purchased from Nilaco (Tokyo, Japan). Pristine WO_3 rods were synthesized by calcination of these tungsten rods in air at 800 °C for 2 h. Ion irradiation of the pristine WO_3 rods was performed using the 300 keV ion accelerator at the High Voltage Electron Microscope Laboratory located at Hokkaido University [31]. The pressure of sample chamber during ion irradiation was ~1.3×10^{-4} Pa. The irradiation was conducted at room temperature with a 100 keV acceleration voltage. These rods were irradiated with H_2^+ ions at a fluence of either 1.0×10^{16} or 1.0×10^{17} ions/cm^2 while He^+ and Ar^+ ions were supplied at a fluence of 5.0×10^{16} and 1.0×10^{16} ions/cm^2, respectively. Samples of both pristine and irradiated WO_3 rods were annealed under vacuum (5.0×10^{-5} Pa) at 500 °C for 4 h. In preparation for cross-sectional micrographs, WO_3 rods were cut using an Isomet low speed saw (Buehler, Illinois, USA).

2.2. Characterization

Parallel beam X-ray diffraction (XRD) analyses were performed by a Smartlab diffractometer using Cu Kα radiation (Rigaku, Tokyo, Japan) to investigate the surface crystal structures of the rods. The grazing incidence angle of 1 ° was applied to the analyses. The morphologies of the rods were also observed by a JSM-7001FA field emission scanning electron microscope (FE-SEM, JEOL, Tokyo, Japan) equipped with an energy dispersive spectroscope (EDS), applying an

accelerating voltage of 15 kV. Chemical bonding states were assessed by an XploRA confocal Raman microscope (Horiba, Kyoto, Japan) with a laser wavelength of 532 nm in conjunction with a 2400 groove/nm grating. Surface chemical bonding states were analyzed by X-ray photoelectron spectrometer (XPS, JEOL, JPS-9200) with Mg Kα radiation. The prepared samples were stored in desiccator decompressed with a rotary pump prior to loading into the spectrometer. The prepared samples were analyzed by some equipments (Raman or XRD) in air, thus samples were exposed to ambient air for less than several hours prior to XPS analysis. In preparation for these assessments, the rods were fixed on a sample holder using carbon tape. The base pressure during spectra acquisition was better than 5.0×10^{-6} Pa achieved by turbomolecular pump. The electron emission angle was 0 ° and the size of sample analyzed area was 1.0 mm in diameter. Sputter-etching or charge neutralizer was not used during the analysis. The binding energy values of the resulting spectra were calibrated by using the work function method [32]. The work function of WO_{3-x} was reported to be 4.7 eV [33], thus the binding energy of C 1s peak was calibrated at 284.88 eV in the present work. Damage profiles following the ion irradiation of WO_3 samples were examined using the Stopping and Range of Ions in Matter (SRIM) program based on calculations performed in the full-cascade mode using the SRIM 2013 software. During these calculations, the sample density and threshold displacement energy values for the W and O sub-lattices were set to 7.16 g/cm^3 and 85 and 40 eV, respectively. Ultraviolet-visible (UV-vis) diffuse reflectance spectra were acquired with a V770 spectrophotometer (JASCO, Tokyo, Japan).

The photocatalytic decomposition of rhodamine 6G (Rh6G) by various specimens was examined under visible light. In these trials, an aqueous solution of Rh6G (10^{-5} M) was prepared. The concentrations of Rh6G in contact with 24 mm rod specimens before and after light exposure were tracked by measuring the absorbance of the solution at the maximum absorbance wavelength of 526 nm using a JASCO V630 spectrophotometer. These trials were performed in quartz cells containing the Rh6G solution and rods. In each case, the cell was allowed to stand in the dark for 60 min to ensure absorption-desorption equilibrium, after which six cycles of 30 min light irradiation per cycle were applied. After each cycle, the rod was removed from the cell and the absorbance of the solution at 526 nm was measured. The cells were irradiated using a 150 W xenon lamp (XEF-152S, KenkoTokina, Tokyo, Japan) with an output of approximately 70,000 lux as determined using an LM-332 digital illuminance meter (AS ONE, Osaka, Japan).

3. Results and discussion

Figure 1 presents photographic images of the tungsten oxide rods used in this study. Figure 1(a) shows the synthesized oxide rods, which exhibited a yellow coloration typical of WO_3. These are referred to herein as the pristine rods. As shown in Fig. 1(b), the oxide rods were masked prior to ion irradiation so that only a selected area was exposed to the ions in each case. Images of oxide rod specimens after ion irradiation at a fluence of 10^{16} ions/cm^2 are provided in Fig. 1(c) and demonstrate that the irradiated areas had an obvious blue color, confirming that selected area ion irradiation was successfully performed. Interestingly, despite using similar fluences, the blue color became darker in the order of H_2^+ to He^+ to Ar^+. During the present work, a normalized grayscale value (NGV) system based on dividing the grayscale value of the blue area by that of the non-irradiated (yellow) area was employed. The NGVs for the specimens irradiated with H_2^+, He^+ and Ar^+ were determined to be 0.48, 0.42, and 0.40, respectively. Figure 1(d) presents images of specimens irradiated with H_2^+ ions at 10^{16} and 10^{17} ions/cm^2. These images confirm that a higher irradiation fluence resulted in a darker blue color. The vacuum annealing of pristine WO_3 rods was found to also change the color of the oxide. but to a deep green as shown in Fig. 1(e).

Variations in the surface structures resulting from ion irradiation were assessed by acquiring parallel beam XRD patterns, and Fig. 2 shows the XRD patterns obtained from both pristine and irradiated WO_3 rods. The noise of the profile of H_2^+-irradiated rod is maybe due to degradation of X-ray tube. The diffraction peaks generated by the pristine rods were indexed to a monoclinic WO_3 phase (PDF# 00-043-1035) and the irradiated samples were also monoclinic phases. Irradiation was expected to generate oxygen-deficient WO_{3-x}, thus a slight change in the profiles were observed, but it was difficult to discuss defects state from the patterns.

Cross-sectional and surface morphologies were observed by scanning electron microscopy (SEM), as shown in Fig. 3. Figure 3(a) and (b) presents cross-sectional and surface images of the pristine WO_3 rods, respectively, and demonstrates that tungsten oxide layers were formed on the outer surfaces of the rods. Interfaces between the outer oxide and inner metal can also be clearly observed in these images, with an estimated oxide thickness of approximately 200 μm. The results of EDS analysis (Fig. S1) showed that oxygen was detected only in the outer surface area. As shown in Fig. 3(b), the pristine WO_3 rods comprised submicron oxide particles. Although the surface morphologies of the vacuum-annealed rods (Fig. 3(c)) and the He^+ irradiated rods (Fig. 3(d)) were similar to that of the pristine material, the morphology after Ar^+ irradiation (Fig. 3(e)

and 3(f)) was somewhat different. As shown in Fig. 3(e), the grain boundaries between oxide particles were not readily apparent following Ar^+ irradiation. This phenomenon is attributed to the Ar^+ sputtering effect. For instance, the effect of re-deposition of the sputtered chemical species would occur. The sputtering yield associated with the present irradiation conditions was calculated using SRIM simulations and values of 5.09 and 0.01 atoms/ion were determined for Ar^+ and He^+ irradiation, respectively. On this basis, sputtering would be expected to occur in the case of Ar^+ irradiation. As shown in Fig. 3(f), some particles were not readily apparent, but others were apparent by Ar^+ irradiation followed by vacuum annealing.

Figure 4 presents the Raman spectra obtained from the pristine and irradiated rods. The pristine sample generated a spectrum containing bands at 716 and 806 cm^{-1} that are ascribed to O-W-O stretching modes [34] along with bands at 272 and 325 cm^{-1} resulting from O-W-O bending modes and a peak at 133 cm^{-1} corresponding to a lattice vibration mode [34]. Although the Raman spectrum of the rods exposed to H_2^+ ions was similar to that of the pristine rods, the spectra generated by the materials treated with He^+ or Ar^+ exhibited peak positions shifted toward lower wavenumbers. In addition, the full width at half maximum of the peaks became broader by ion irradiation. Raman peaks shifts and broadening caused by oxygen vacancies have previously been observed in metal oxide systems [35,36]. Thus, the results of our study suggest that oxygen vacancies were formed during irradiation with either He^+ or Ar^+ ions.

Figure 5 provides XPS wide-scan spectra of pristine, vacuum-annealed and irradiated rods, which showed the existence of carbon, oxygen and tungsten element in all specimens. The irradiated rods showed the stronger C 1s peak intensities compared with those of pristine and vacuum-annealed rods. In particular, He^+ irradiated rods, which has the largest fluence value, showed the strongest C 1s peak intensity among irradiated rods. The increase of carbon peak intensity was caused by surface contamination introduced during ion irradiation, which was also confirmed in our previous study of Cu system [29, 30]. The carbon contamination of the rods exposed to Ar^+ ions was reduced by subjecting the material to vacuum annealing (see the spectra labeled Ar^+_Vac. 500 °C rod in Fig. 5). In addition, the low intensity Si 2s and 2p peaks were detected in the spectra of irradiated rods except the rod exposed to H_2^+ ions. The silicon species would also originate from the contamination during ion irradiation. The origin of Si and C would be the residual gas of silicone oil and/or sample fixture in the irradiation chamber. Figure 6 shows the core-level spectra of the prepared tungsten oxide rods. Fig. 6(a) shows W 4f spectra. As shown

in Fig. 6(a), the spectrum of the pristine WO_3 rods exhibits W $4f_{7/2}$ and W $4f_{5/2}$ spin-orbit doublet peaks at 35.3 and 37.4 eV, respectively, corresponding to the W^{6+} oxidation state. In the spectra obtained from the vacuum-annealed rod (Fig. 6(a)), the W $4f_{7/2}$ and $4f_{5/2}$ peaks were slightly shifted to higher energies (a shift of 0.2 eV). This shift would be caused by oxygen vacancies formation by segregation of oxygen toward the surface during vacuum annealing [37,38]. For pristine, vacuum-annealed, H_2^+-irradiated and Ar^+-irradiated rods, peak fitting analyses were carried out and the results were shown in Fig. S2. In the previous study, the doublet peaks corresponding to W^{5+} peaks were observed for ion-irradiated WO_3 [14,18]. The increase in the relative proportion of W^{5+} species following Ar^+ irradiation indicates that ion irradiation generated a large number of oxygen vacancies compared with vacuum-annealed rod. In the case of H_2^+ irradiation, the formation of both H_xWO_3 and oxygen vacancies could occur. The results of a previous study suggested that the production of H_xWO_3 was the dominant carrier-generation mechanism in WO_3 during H^+ ion irradiation [11]. Further study on depth-dependent analyses of bonding states would be needed to clarify the H_xWO_3 species, which was characterized in a recent study [39]. In contrast to vacuum annealing, ion irradiation causes depth-dependent vacancy distributions, and Fig. S3 provides depth profiles of tungsten and oxygen vacancies following 100 keV irradiation as simulated using the SRIM program. It is apparent from Fig. S3(a) and (b) that higher concentrations of oxygen vacancies should be formed compared with tungsten vacancies and the maximum damage was predicted to occur at depths of approximately 400 and 50 nm in conjunction with He^+ and Ar^+ irradiation, respectively. The defects information in bulk is important for considering the photocatalytic properties, which will be discussed later.

Fig. 6(b) shows the XPS spectra of O 1s. The peak at 530.1 eV seen in the spectrum of the pristine rods corresponds to lattice oxygen in WO_3 [40] and the spectrum acquired from the vacuum-annealed rods showed the peak at 530.3 eV, meaning that this peak was slightly shifted to higher binding energy compared with the pristine rods. This shift of O 1s spectra was consistent with the shift of W 4f spectra. The H_2^+-, He^+- and Ar^+-irradiated rods showed the similar lattice oxygen peak in addition to a new peak at 532.3 eV that would be attributed to C-O and C=O species [41]. This species would be formed by surface contamination by ion irradiation and the following air exposure. The XPS spectra of C 1s are shown in Fig. 6(c). The Ar^+-irradiated specimens were subjected to vacuum annealing and the W 4f and O 1s spectra of this material are shown in the bottom of Fig. 6(a) and (b), respectively. The W 4f peaks and lattice oxygen peak of

O 1s were shifted to higher binding energy compared with the pristine rods or rods treated with vacuum annealing but not irradiation. Compared with surface contamination peak at 532.8 eV, the lattice oxygen peak at 531.0 eV showed strong intensities. The shift of peak to higher binding energy is ascribed to the presence of WO_{3-x} phases in the rods. The diffusion of interstitials and vacancies during vacuum annealing would be expected to modify the surface structures of these rods to form WO_{3-x} phases. The appearance of a sharp lattice oxygen peak after vacuum annealing is an important result with regard to potential applications of ion-irradiated WO_3 to SERS. In previous research, the Ar^+ irradiation of a WO_3 film followed by vacuum annealing enhanced the sensitivity with which this oxide responded to dye molecules during SERS, whereas ion irradiation without the annealing did not have this effect [17]. The XPS spectra indicate that carbon contaminations covered the irradiated surfaces of the rods, and these species could possibly impede charge transfer between the WO_{3-x} surface and dye molecules. However, vacuum annealing would enhance the effectiveness of surface lattice oxygen species, which would be conducive to charge transfer between adsorbed molecules and the oxide.

The photocatalytic properties of the prepared tungsten oxide rods were evaluated under visible light and Fig. 7(a) plots the relative Rh6G concentration (C/C_0) values over time. The photocatalytic decomposition kinetics of Rh6G can be explained by pseudo first-order kinetics with the equation of $\ln(C_0/C) = kt$ (k: reaction rate constant, t: time) [21]. The photocatalytic decomposition plots of Rh6G in Fig. 7(a) followed the pseudo first-order kinetics model as shown in Fig. S4. The photocatalytic efficiency of the rods irradiated with H_2^+ at a fluence of 10^{16} ions/cm^2 was lower than that of the pristine WO_3 rods. The surface carbon contamination of the rods exposed to Ar^+ ions, as well as the concentration of irradiation-induced defects, was reduced by subjecting the material to vacuum annealing (see the line labeled Ar^+_Vac. 500 °C rod in Fig. 7(a)) and then evaluating the photocatalytic properties. However, the photocatalytic efficiency of this material was also lower than that of the pristine rods. It is known that oxygen vacancies in WO_3 often act as recombination centers for electrons and holes during photocatalysis [26] and so oxygen vacancies formed by ion irradiation would be expected to decrease photocatalytic efficiency. In contrast, vacuum-annealed rods without ion irradiation showed higher photocatalytic efficiency than that of the pristine rods, suggesting that the catalytic properties could be modified by varying the method by which oxygen vacancies are introduced. The better photocatalytic properties of vacuum-annealed rods were also confirmed by the photocatalytic tests with short-length specimens

as shown in Fig. S5. Fig. 7(b) shows the UV-vis diffuse reflectance spectra of tungsten oxide powders scraped off the rod surfaces. These spectra demonstrate that visible light absorption above 470 nm was improved after vacuum annealing. Similar absorption properties were also previously reported for other blue-green tungsten oxide samples containing high concentrations of oxygen vacancies [21,26,36].

On the basis of the above results, we concluded that the vacuum-annealed green rods exhibited enhanced absorption in the visible light region as a consequence of the small amount of contaminations and oxygen vacancies on the rod surfaces, which in turn provided high photocatalytic efficiency. Although ion irradiation also would enhance the visible light absorption properties of the rods, numerous oxygen vacancies were formed on the surfaces and in the bulk of the materials. Therefore, electron-hole recombination would occur such that the photocatalytic efficiency would be reduced [26]. Also, irradiation-induced carbon and silicon contamination would inhibit the contact between oxide surfaces and dyes, which also results in the low efficiency. Although the present irradiation conditions did not improve the photocatalytic properties, optimizing the irradiation parameters could potentially induce enhanced catalysis. As an example, the SERS sensitivity of WO_3 thin films exposed to Ar^+ ions has been found to depend on the irradiation conditions [17]. In addition, it should be noted that the photocatalytic properties of TiO_2 system under ultraviolet irradiation can be improved by gas phase ion irradiation [42].

4. Conclusion

Tungsten oxide rods irradiated with H_2^+, He^+ or Ar^+ ions and subjected to vacuum annealing were prepared. This is the first report of a complete evaluation of XPS spectra of ion-irradiated WO_3 surface. Vacuum annealing caused shifts of W 4f and O 1s peaks to higher binding energies, and increased the proportion of W^{5+} slightly, indicating the lesser amounts of surface oxygen vacancies. The XPS wide-scan spectra showed that the surfaces of irradiated areas were contaminated with carbon and silicon species. The higher irradiation fluence caused the formation of more contamination, thus the contaminations were introduced during ion irradiation process. As a result of O 1s core-level spectra, a characteristic peak of contamination was appeared at ~532.3 eV in addition to a lattice oxygen peak. Vacuum annealing at 500 °C decreased the carbon contamination and increased the lattice oxygen species associated with a surface WO_{3-x} phase. The increase of lattice oxygen species would be important with regard to potential applications of ion-irradiated

WO_3 to SERS. The visible light photocatalytic decomposition of rhodamine 6G was first reported for ion-irradiated WO_3. Samples in which WO_{3-x} was generated by irradiation exhibited low photocatalytic efficiencies even when the contamination was decreased by vacuum annealing. Vacuum-annealed green WO_{3-x} rods showed high photocatalytic efficiency as a consequence of the enhanced absorption of visible light and low concentration of contamination and vacancies. In the present study, irradiation-induced surface contamination was detected. Therefore, in addition to oxygen vacancies, contamination effects should be carefully evaluated for the photocatalytic or SERS applications of WO_3 in the future study.

AUTHOR INFORMATION

Corresponding Author

* Corresponding author. Tel.: +81 11 706 7134

E-mail addresses: y-nakagawa@eng.hokudai.ac.jp (Y. Nakagawa)

Declaration of Competing Interest

The authors declare that they have no known competing financial interest.

Acknowledgments

This work was supported by JSPS KAKENHI grant number 20H00295. Part of this work was conducted at the joint-use facilities in Hokkaido University, supported by the Nanotechnology Platform (grant number JPMXP09A21HK0021) and the Project for Promoting Public Utilization of Advanced Research Infrastructure (Program for Supporting Introduction of the New Sharing System) (grant number JPMXS0420100520). The authors thank Dr. Shuntaro Murakami and Prof. Seiichi Watanabe for providing assistance during sample synthesis and diffuse reflectance spectroscopy experiments. We thank Edanz (https://jp.edanz.com/ac) for editing a draft of this manuscript.

References

[1] O. Samuel, M. H. D. Othman, R. Kamaludin, O. Sinsamphanh, H. Abdullah, M.H. Puteh, T. A. Kurniawan, WO_3-based photocatalysts: A review on synthesis, performance enhancement and photocatalytic memory for environmental applications, Ceram. Int. 48 (2022) 5845-5875. https://doi.org/10.1016/j.ceramint.2021.11.158.

[2] J.C. Murillo-Sierra, A. Hernandez-Ramirez, L. Hinojosa-Reyes, J.L. Guzman-Mar, A review on the development of visible light-responsive WO_3-based photocatalysts for environmental applications, Chem. Eng. J. Adv. 5 (2021) 100070. https://doi.org/10.1016/j.ceja.2020.100070

[3] C. Dong, R. Zhao, L. Yao, Y. Ran, X. Zhang, Y. Wang, A review on WO_3 based gas sensors: Morphology control and enhanced sensing properties, J. Alloys Compd. 820 (2020) 153194. https://doi.org/10.1016/j.jallcom.2019.153194.

[4] S. Cong, Y. Yuan, Z. Chen, J. Hou, M. Yang, Y. Su, Y. Zhang, L. Li, Q. Li, F. Geng, Z. Zhao, Noble metal-comparable SERS enhancement from semiconducting metal oxides by making oxygen vacancies, Nat. Commun. 6 (2015) 7800. https://doi.org/10.1038/ncomms8800.

[5] G. Barbillon, Latest Novelties on Plasmonic and Non-Plasmonic Nanomaterials for SERS Sensing, Nanomaterials 10 (2020) 1200. https://doi.org/10.3390/nano10061200.

[6] S. Wang, W. Fan, Z. Liu, A. Yu, X. Jiang, Advances on tungsten oxide based photochromic materials: strategies to improve their photochromic properties, J. Mater. Chem. C 6 (2018) 191-212. https://doi.org/10.1039/c7tc04189f.

[7] S. Murakami, L. Zhang, M. Jeem, K. Okamoto, Y. Nakagawa, T. Shibayama, M. Ohnuma, S. Watanabe, Photo- & radio-chromic iron-doped tungstic acids fabricated *via* submerged photosynthesis, Opt. Mater. 124 (2022) 111966. https://doi.org/10.1016/j.optmat.2021.111966.

[8] W. Pu, Z. Song, J. Yan, H. Xu, H. Ji, S. Yuan, H. Li, Preparation of oxygen-deficient 2D WO_{3-x} nanoplates and their adsorption behaviors for organic pollutants: equilibrium and kinetics modeling, J. Mater. Sci. 54 (2019) 12463-12475. https://doi.org/10.1007/s10853-019-03780-6.

[9] Kriti, P. Kaur, S. Kaur, D. Arora, K. Asokan, D.P. Singh, Influence of defect structure on colour tunability and magneto optical behaviour of WO_3 nanoforms, RSC Adv. 9 (2019) 20536. https://doi.org/10.1039/c9ra01901d.

[10] Z. S. Houweling, J.W. Geus, R. E. I. Schropp, Hot-wire chemical vapor deposition of WO_{3-x} thin films of various oxygen contents, Mater. Chem. Phys. 140 (2013) 89-96. https://doi.org/10.1016/j.matchemphys.2013.02.072.

[11] M. Miyakawa, K. Ueda, H. Hosono, Carrier generation in highly oriented WO_3 films by proton or helium implantation, J. Appl. Phys. 92 (2002) 2017-2022. https://doi.org/10.1063/1.1496120.

[12] M. Miyakawa, K. Kawamura, H. Hosono, H. Kawazoe, Large electrical conductivity enhancement of WO_3 thin films produced by ion implantation, J. Appl. Phys. 84 (1998) 5610-5613. https://doi.org/10.1063/1.368608.

[13] X. D. Zheng, F. Ren, H. Y. Wu, W. J. Qin, C. Z. Jiang, Formation of tungsten oxide nanowires by ion irradiation and vacuum annealing, Nanotechnology 29 (2018) 155301. https://doi.org/10.1088/1361-6528/aaac09.

[14] X. D. Zheng, The influence of ion implantation-induced oxygen vacancy on electrical conductivity of WO_3 thin films, Vacuum 165 (2019) 46-50. https://doi.org/10.1016/j.vacuum.2019.04.004.

[15] Y. Sugawara, Y. Sakaizawa, A. Shibata, I. Muto, N. Hara, Detection of hydrogen distribution in pure iron using WO_3 thin film, ISIJ Int. 58 (2018) 1860-1867. https://doi.org/10.2355/isijinternational.ISIJINT-2018-236.

[16] S. Murakami, L. Zhang, S. Watanabe, Visualization of aquaionic splitting *via* iron corrosion, Sci. Rep. 10 (2020) 1726. https://doi.org/10.1038/s41598-020-58707-y.

[17] X. D. Zheng, F. Ren, S. Zhang, X. Zhang, H. Wu, X. Zhang, Z. Xing, W. Qin, Y. Liu, C. Jiang, A General Method for Large-Scale Fabrication of Semiconducting Oxides with High SERS Sensitivity, ACS Appl. Mater. Interfaces 9 (2017) 14534-14544. https://doi.org/10.1021/acsami.7b03839.

[18] X. D. Zheng, L. Wu, F. Ren, Oxygen vacancy enhanced room temperature ferromagnetism in Ar^+ ion irradiated WO_3 films, Ceram. Int. 47 (2021) 5091-5098. https://doi.org/10.1016/j.ceramint.2020.10.087.

[19] S. Keshri, A. Kumar, D. Kabiraj, Tailoring of optical and gas sensitivity behaviors of WO_3 films by low energy Ar^+ ion implantation, Thin Solid Films 526 (2012) 50-58. https://doi.org/10.1016/j.tsf.2012.10.101.

[20] F.Y. Xie, L. Gong, X. Liu, Y.T. Tao, W.H. Zhang, S.H. Chen, H. Meng, J. Chen, XPS studies on surface reduction of tungsten oxide nanowire film by Ar^+ bombardment, J. Electron Spectrosc. Relat. Phenom. 185 (2012) 112-118. https://doi.org/10.1016/j.elspec.2012.01.004.

[21] Y. Ishida, S. Motono, W. Doshin, T. Tokunaga, H. Tsukamoto, T. Yonezawa, Small Nanosized Oxygen-Deficient Tungsten Oxide Particles: Mechanistic Investigation with Controlled Plasma Generation in Water for Their Preparation, ACS Omega 2 (2017) 5104-5110. https://doi.org/10.1021/acsomega.7b00986.

[22] F.G. Rinaldi, O. Arutanti, A.F. Arif, T. Hirano, T. Ogi, K. Okuyama, Correlations between Reduction Degree and Catalytic Properties of WO_x Nanoparticles, ACS Omega 3 (2018) 8963-8970. https://doi.org/10.1021/acsomega.8b01110.

[23] S. Chen, Y. Xiao, W. Xie, Y. Wang, Z. Hu, W. Zhang, H. Zhao, Facile Strategy for Synthesizing Non-Stoichiometric Monoclinic Structured Tungsten Trioxide (WO_{3-x}) with Plasma Resonance Absorption and Enhanced Photocatalytic Activity, Nanomaterials 8 (2018) 553. https://doi.org/10.3390/nano8070553.

[24] S. Rahimnejad, J.H. He, F. Pan, X. Lee, W. Chen, K. Wu, G.Q. Xu, Enhancement of the photocatalytic efficiency of WO_3 nanoparticles via hydrogen plasma treatment, Mater. Res. Express 1 (2014) 045044. https://doi.org/10.1088/2053-1591/1/4/045044.

[25] D. Fukushi, A. Sasaki, H. Hirabayashi, M. Kitano, Effect of oxygen vacancy in tungsten oxide on the photocatalytic activity for decomposition of organic materials in the gas phase, Microelectron. Reliab. 79 (2017) 1-4. https://doi.org/10.1016/j.microrel.2017.09.025.

[26] Q. Liu, F. Wang, H. Lin, Y. Xie, N. Tong, J. Lin, X. Zhang, Z. Zhang, X. Wang, Surface oxygen vacancy and defect engineering of WO_3 for improved visible light photocatalytic performance, Catal. Sci. Technol. 8 (2018) 4399-4406. https://doi.org/10.1039/c8cy00994e.

[27] J. Král, J. Zemek, Carbon contamination of ion implanted layers, Vacuum 36 (1986) 555-557. https://doi.org/10.1016/0042-207X(86)90247-2.

[28] G.S. Was, S. Taller, Z. Jiao, A.M. Monterrosa, D. Woodley, D. Jennings, T. Kubley, F. Naab, O. Toader, E. Uberseder, Resolution of the carbon contamination problem in ion irradiation experiments, Nucl. Instrum. Methods Phys. Res. B 412 (2017) 58-65. https://doi.org/10.1016/j.nimb.2017.08.039.

[29] S. Yang, Y. Nakagawa, T. Shibayama, An investigation of surface contamination introduced during He^+ implantation and subsequent effects on the thermal oxidation of Cu, Appl. Surf. Sci. 579 (2022) 152163. https://doi.org/10.1016/j.apsusc.2021.152163.

[30] S. Yang, Y. Nakagawa, T. Shibayama, Tailored copper oxidation in alkaline aqueous solution after helium cation implantation, Appl. Surf. Sci. 591 (2022) 153087. https://doi.org/10.1016/j.apsusc.2022.153087.

[31] J. Ishioka, K. Kogure, K. Ofuji, K. Kawaguchi, M. Jeem, T. Kato, T. Shibayama, S. Watanabe, In situ direct observation of photocorrosion in ZnO crystals in ionic liquid using a laser-equipped high-voltage electron microscope, AIP Advances 7 (2017) 035220. https://doi.org/10.1063/1.4979726.

[32] G. Greczynski, L. Hultman, Reliable determination of chemical state in x-ray photoelectron spectroscopy based on sample-work-function referencing to adventitious carbon: Resolving the myth of apparent constant binding energy of the C 1s peak, Appl. Surf. Sci. 451 (2018) 99-103. https://doi.org/10.1016/j.apsusc.2018.04.226.

[33] S.Y. Lee, G. Shim, J. Park, H. Seo, Tunable polaron-induced coloration of tungsten oxide via a multi-step control of the physicochemical property for the detection of gaseous F, Phys. Chem. Chem. Phys. 20 (2018) 16932. https://doi.org/10.1039/c8cp00158H.

[34] K. Thummavichai, N. Wang, F. Xu, G. Rance, Y. Xia, Y. Zhu, *In situ* investigations of the phase change behaviour of tungsten oxide nanostructures, R. Soc. Opensci. 5 (2018) 171932. https://doi.org/10.1098/rsos.171932.

[35] S. Soni, S. Kumar, B. Dalela, S. Kumar, P.A. Alvi, S. Dalela, Defects and oxygen vacancies tailored structural and optical properties in CeO_2 nanoparticles doped with Sm^{3+} cation, J. Alloys Compd. 752 (2018) 520-531. https://doi.org/10.1016/j.jallcom.2018.04.157.

[36] Y. Li, C. Wang, H. Zheng, F. Wan, F. Yu, X. Zhang, Y. Liu, Surface oxygen vacancies on WO_3 contributed to enhanced photothermo-synergistic effect, Appl. Surf. Sci. 391 (2017) 654-661. https://doi.org/10.1016/j.apsusc.2016.07.042.

[37] T.G.G. Maffeis, M.W. Penny, R.J. Cobley, E. Comini, G. Sberveglieri, S.P. Wilks, XPS Characterisation of vacuum annealed nanocrystalline WO_3 films, e-J. Surf. Sci. Nanotech. 7 (2009) 319-322. https://doi.org/10.1380/ejssnt.2009.319.

[38] S. Santucci, L. Lozzi, E. Maccallini, M. Passacantando, L. Ottaviano, C. Cantalini, Oxygen loss and recovering induced by ultrahigh vacuum and oxygen annealing on WO_3 thin film

surfaces: Influences on the gas response properties, J. Vac. Sci. Technol. A 19 (2001) 1467-1473. https://doi.org/10.1116/1.1349190.

[39] Y. Tang, S. Gan, L. Zhong, Z. Sun, L. Xu, C. Liao, K. Lin, X. Cui, D. He, Y. Ma, W. Wang, L. Niu, Lattice proton intercalation to regulate WO_3-based solid-contact wearable pH sensor for sweat analysis, Adv. Funct. Mater. 32 (2022) 2107653.

[40] A.P. Shpak, A.M. Korduban, M.M. Medvedskij, V.O. Kandyba, XPS studies of active elements surface of gas sensors based on WO_{3-x} nanoparticles, J. Electron Spectros. Relat. Phenomena 156-158 (2007) 172-175. https://doi.org/10.1016/j.elspec.2006.12.059.

[41] G. Greczynski, L. Hultman, X-ray photoelectron spectroscopy: Towards reliable binding energy referencing, Prog. Mater. Sci. 107 (2020) 100591. https://doi.org/10.1016/j.pmatsci.2019.100591.

[42] Z. Li, Y. Teng, C. Chen, S. Lv, G. Wang, Z. Zhang, Effect of Xe ion irradiation on photocatalytic performance of oblique TiO_2 nanowire arrays, Appl. Surf. Sci. 327 (2015) 478-482. https://doi.org/10.1016/j.apsusc.2014.12.009.

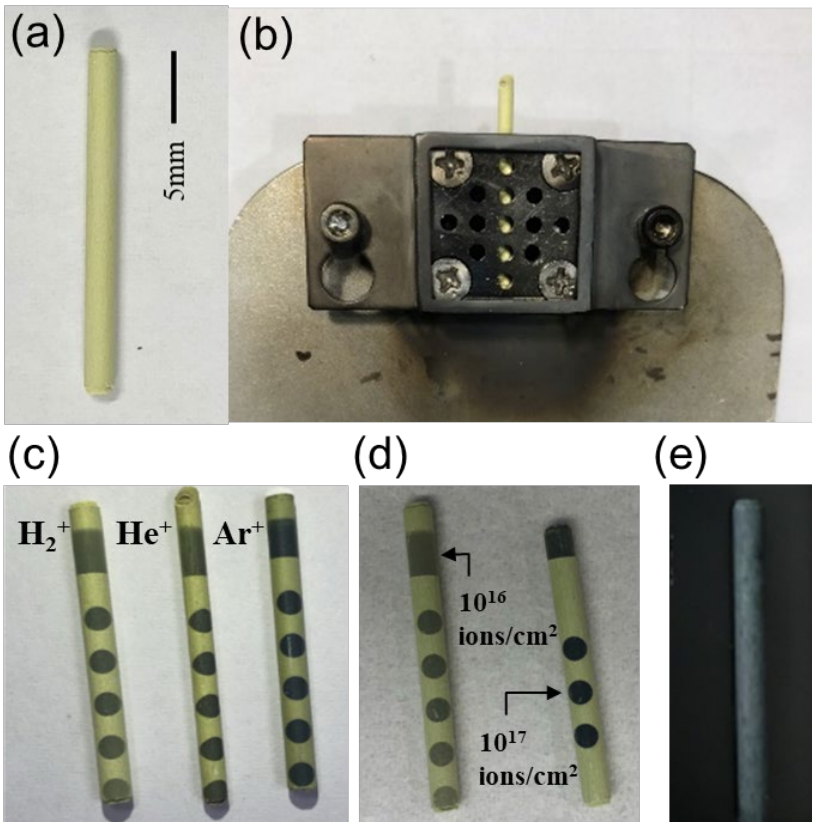

444 Fig. 1. Photographic images of fresh and ion-irradiated tungsten oxide rods. (a) A freshly
445 synthesized (pristine) rod, (b) an oxide rod in the mask used during ion irradiation, (c) rods
446 irradiated over selected areas at a fluence on the order of 10^{16} ions/cm^2, (d) rods irradiated with
447 H_2^+ ions using different fluences, and (e) a rod after vacuum annealing at 500 °C for 4 h. Due to
448 the unclear sample color on a white background, black background was used for vacuum-annealed
449 rod.

450

451

452

453

454

455

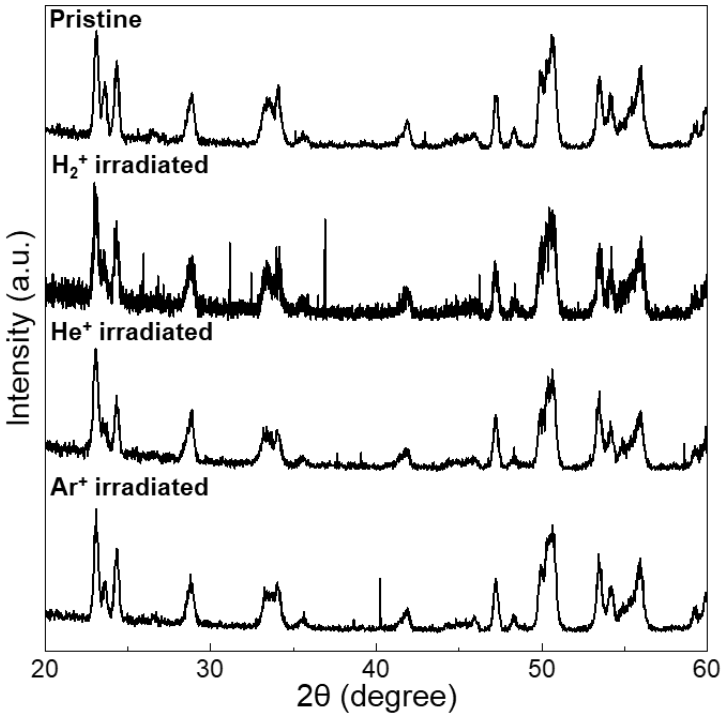

Fig. 2. Parallel beam X-ray diffraction profiles of pristine and irradiated tungsten oxide rods.

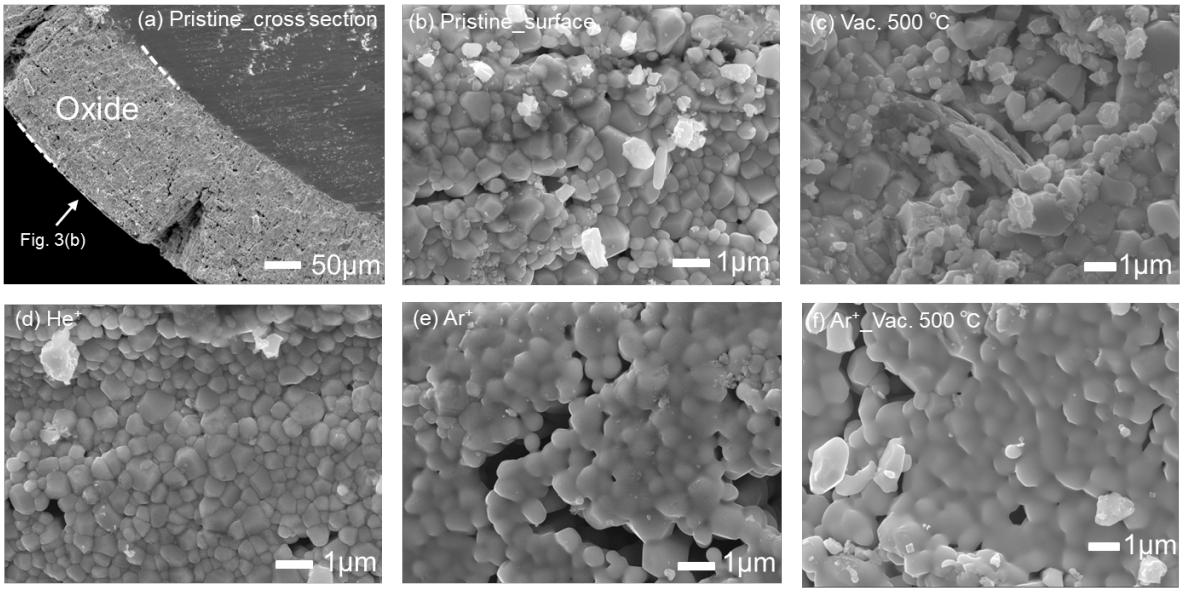

Fig. 3. Cross-sectional and surface SEM images of tungsten oxide rods. (a, b) A pristine rod, (c) a vacuum-annealed rod without ion irradiation, (d, e) an ion-irradiated rod, and (f) a rod irradiated with Ar^+ followed by vacuum annealing. Images acquired at an acceleration voltage of 15 kV. In the Fig. 3(a), oxide thickness was ~200 μm. The arrow in the Fig. 3(a) indicates the observation direction of the Fig. 3(b).

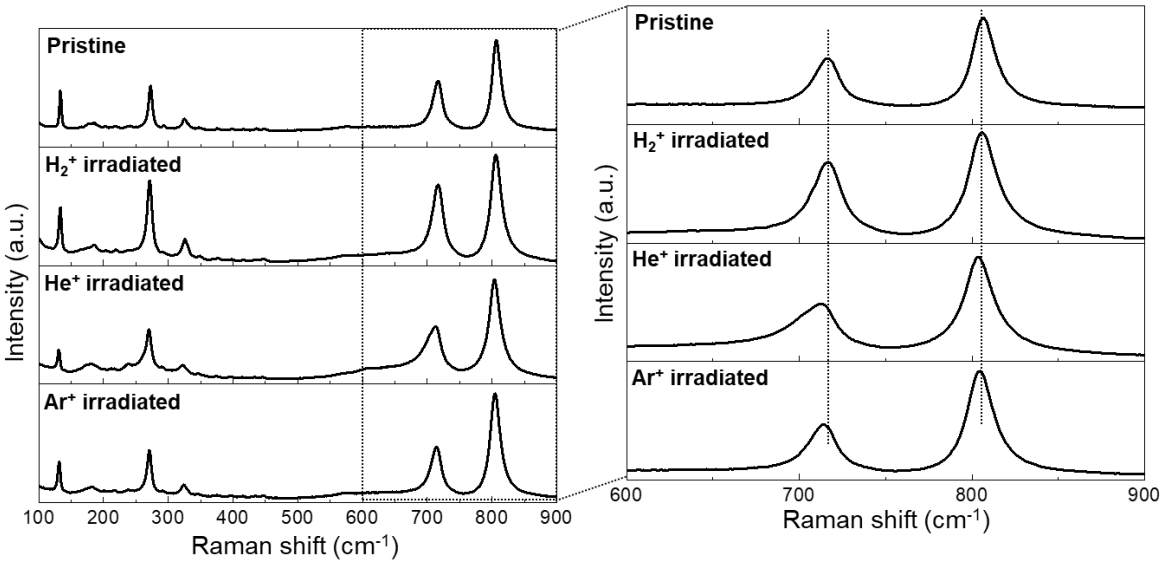

Fig. 4. Raman spectra of various tungsten oxide rod specimens.

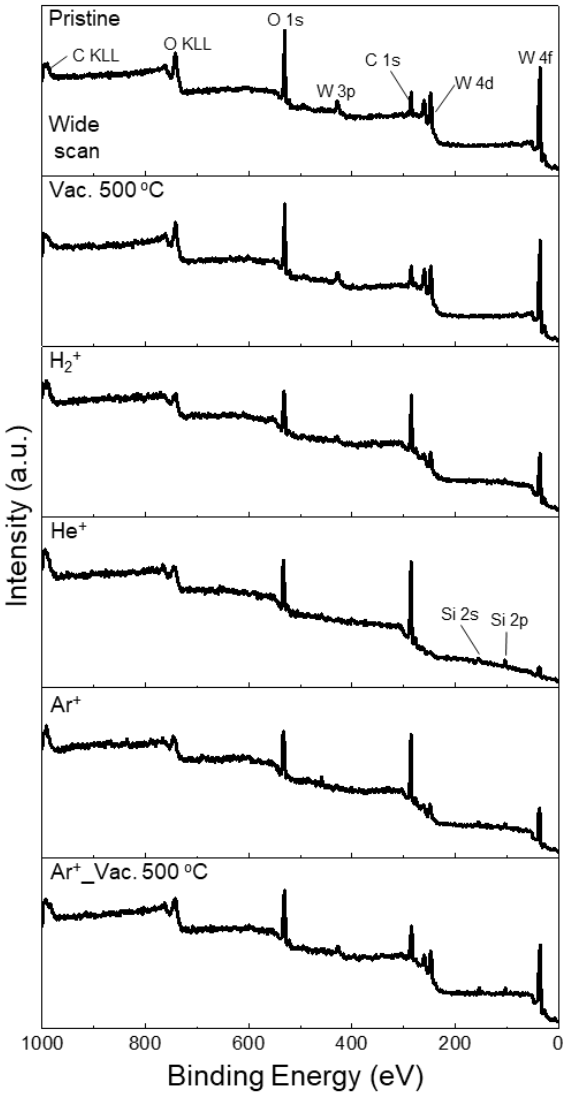

507

508 Fig. 5. XPS wide-scan spectra obtained from various tungsten oxide rod specimens.

509

510

511

512

513

514

515

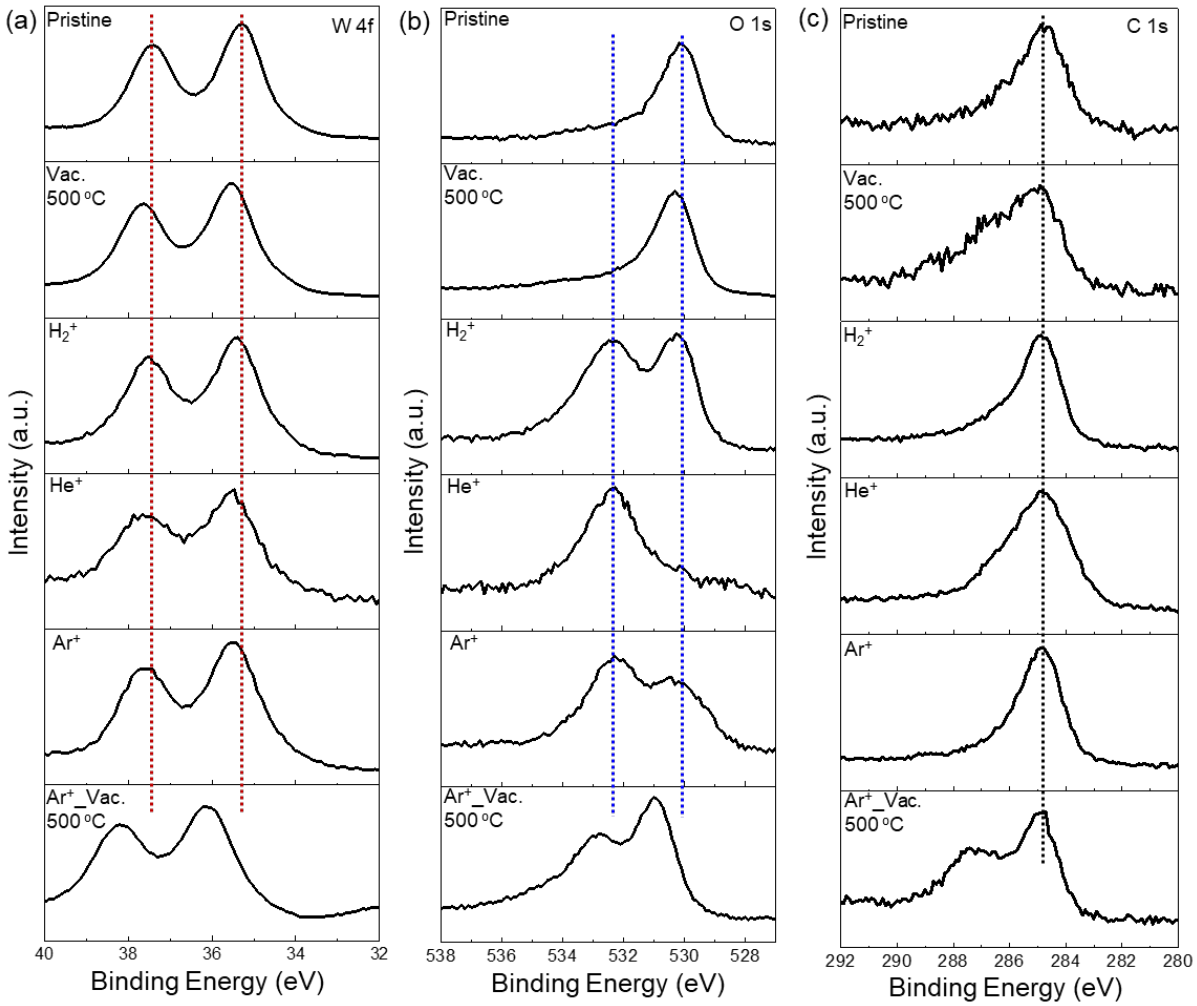

Fig. 6. XPS core-level spectra obtained from various tungsten oxide rod specimens. (a) W 4f spectra, (b) O 1s spectra, and (c) C 1s spectra.

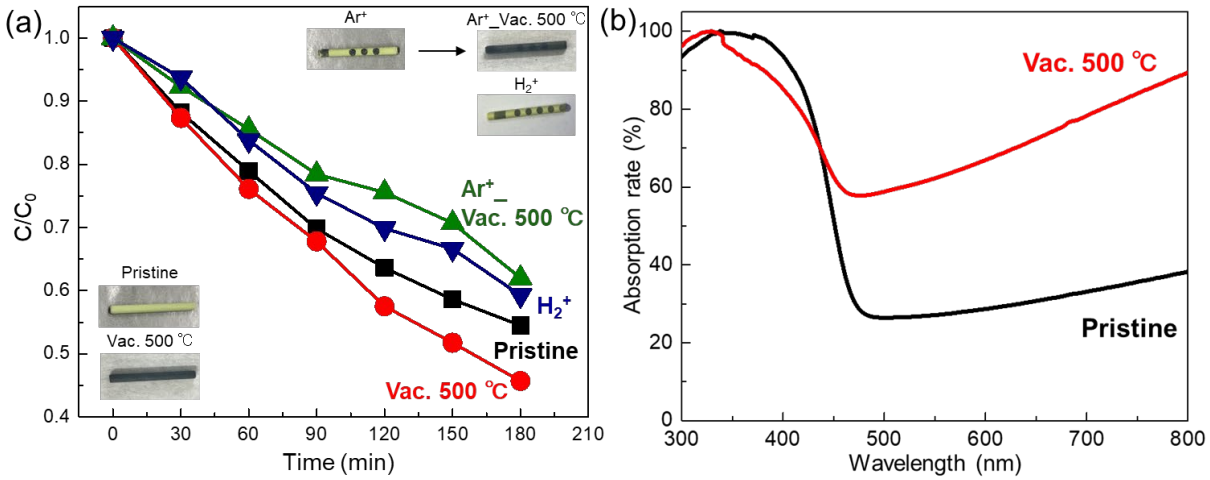

527

528 Fig. 7. (a) Plots showing the photocatalytic degradation of rhodamine 6G in aqueous solution by
529 tungsten oxide rods exposed to visible light. The insets show photographic images of the samples
530 used for the photocatalytic tests (The picture of Ar^+ is shown to indicate the irradiated area). (b)
531 UV-vis diffuse reflectance spectra of tungsten oxide powders scraped off rods.